Article

Scanning Nitrogen-Vacancy Magnetometry of Focused-Electron-Beam-Deposited Cobalt Nanomagnets

Liza Žaper, Peter Rickhaus, Marcus Wyss, Boris Gross, Kai Wagner, Martino Poggio, and Floris Braakman*

Read Online

ACCESS | Metrics & More | Article Recommendations | Supporting Information

ABSTRACT: Focused-electron-beam-induced deposition is a promising technique for patterning nanomagnets in a single step. We fabricate cobalt nanomagnets in such a process and characterize their content, saturation magnetization, and stray magnetic field profiles by using a combination of transmission electron microscopy and scanning nitrogen-vacancy (NV) magnetometry. We find agreement between the measured stray field profiles and saturation magnetization with micromagnetic simulations. We further characterize magnetic domains and grainy stray magnetic fields in the nanomagnets and their halo side-deposits. This work may aid in the evaluation of Co nanomagnets produced through focused electron-beam-induced deposition for applications in spin qubits, magnetic field sensing, and magnetic logic.

KEYWORDS: *FEBID, cobalt, nanostructures, scanning probe microscopy, magnetic properties, spin qubits*
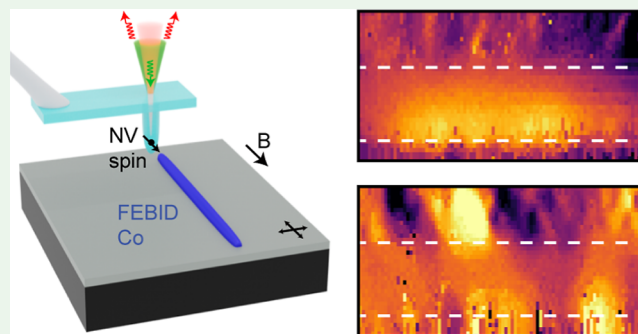
INTRODUCTION

Nanomagnets with precisely defined geometries are of interest for a variety of applications, including magnetic resonance force microscopy,[1,2] as mediating elements between spins and mechanical degrees of freedom,[3–5] magnetic memories,[6] and nanomagnet logic[7] and for the implementation of quantum logic with spin-based qubits[8,9] such as electron spins confined in quantum dots. Typically, nanomagnets are patterned using a multistep procedure, involving resist-coating, electron-beam lithography, deposition of a thin film of a magnetic material such as cobalt, and lift-off. High-quality thin films of Co can be deposited in various ways, including ion beam sputtering,[10] electron-beam evaporation,[11] thermal evaporation,[11,12] electrolytic deposition,[13] metal−organic chemical vapor deposition (MOCVD),[14] molecular beam epitaxy (MBE),[15] and pulsed laser deposition (PLD).[16] Such a multistep patterning procedure is prone to introducing impurities in the devices in the form of residual resist particles as well as causing possible misalignment. Furthermore, such techniques are limited to the fabrication of 2D patterns.

Here, we use focused-electron-beam-induced deposition (FEBID) to pattern Co nanomagnets.[17] FEBID is an appealing technique for the fabrication of nanomagnets due to its single-step nature and allows for the fabrication of 3D geometries,[18] opening up new ways of engineering magnetic gradients optimized for spin qubit control. For example, such 3D patterning could be used to produce arrays of nanomagnets with identical 2D footprints but differing in height profile. Such

arrays would be of use in scaling up, e.g., spin qubit devices in a modular approach, where variations in the nanomagnet height profile can be used to locally vary the spin qubit Zeeman energy and/or magnetic field gradients, allowing for individual qubit addressability as well as variations in driving and dephasing strengths across the arrays. Another potential advantage of FEBID to pattern nanomagnets lies in its direct-write nature. This allows for in situ fine-tuning of the shape and magnetic properties, such as coercivity and magnetic anisotropy, of the deposits. Furthermore, FEBID does not generate impurities in the form of residual resist, although C and O are typically deposited along with Co. FEBID of Co has been demonstrated as a reliable technique for growing highly magnetic nanostructures, reaching Co content of up to ∼96 atomic percent of bulk values.[17,19] FEBID also allows for patterning with lateral resolution in the nm range,[20] approaching the intrinsic limit of the process imposed by the electron beam diameter.[21,22] For Co nanostructures, lateral resolutions of below 30 nm have thus far been achieved.[23]
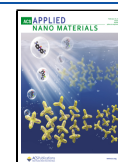
We characterize the properties of FEBID nanomagnets using high-angle annular dark-field scanning transmission electron
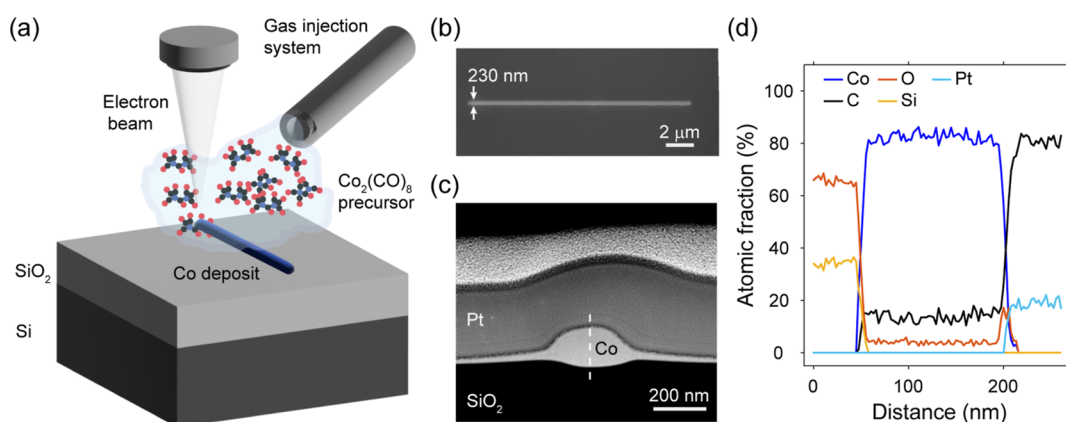
Figure 1. (a) Illustration describing FEBID patterning of a Co nanomagnet. (b) SEM image of the Co nanomagnet studied here. (c) HAADF-STEM image of a cross-section of a Co nanowire (NW) nanomagnet, similar to the magnets studied here. (d) EDS analysis along the line cut shown in (c).

microscopy (HAADF-STEM), high-resolution energy dispersive spectroscopy (EDS) analysis, and atomic force microscopy (AFM). We use scanning nitrogen-vacancy center magnetometry (SNVM)[24] to image the stray magnetic field of the Co deposits, both at externally applied magnetic field sufficiently high to achieve magnetization saturation and at a low field. We find good agreement between our measurements and micromagnetic simulations. Spatial characterization of nanomagnet stray fields is important to evaluate the use of these nanomagnets for the mentioned applications. Such a characterization helps in determining detrimental effects, such as impurity levels and disordered stray magnetic fields. In particular, when they are used to control spin qubits, it is relevant to estimate the effect of disordered magnetic fields on qubit decohering mechanisms. From our SNVM measurements of the disordered stray magnetic field of unintended deposits surrounding the nanomagnet, we estimate spin qubit dephasing times in the presence of charge noise.

The sketch in Figure 1a illustrates the working principle of our FEBID[25−28] fabrication technique. First, a precursor molecule containing cobalt, $Co_2(CO)_8$, is introduced inside a chamber pumped to a high vacuum. Irradiating the precursor molecules adsorbed on the sample surface with an electron beam causes them to decompose, leaving the nanostructured Co deposits on the exposed areas of the sample substrate.[17] By directing the beam using a scanning electron microscope, this technique can be used to, in a single step, pattern Co nanodeposits with high resolution.[23]

To grow the nanomagnets, we used a commercial Thermo Fisher FEI Helios 650 NanoLab FIB/ scanning electron microscope, equipped with a $Co_2(CO)_8$ gas injection system. We use a GIS tip with a round nozzle with a diameter of 300 μm. The tip is positioned 120 μm above the sample surface and at a lateral distance of 85 μm from the deposition area. The nanomagnets are patterned on the top surface of a Si substrate covered with 290 nm of thermally grown SiO_2. We fabricate nanomagnets with a nanowire (NW) shape in order to obtain a magnetic configuration with a single magnetic easy axis, enabling alignment to the sensitive axis [nitrogen-vacancy (NV) center quantization axis] of our scanning probe and straightforward comparison to simulations. To achieve high Co content and high lateral resolution, we used the following FEBID parameters:[17] an acceleration voltage of 10 kV, a beam current of 3.2 nA, a dwell time of 1 μs, and a precursor flux

corresponding to a vacuum chamber pressure of 4×10^{-6} mbar. We have achieved patterning Co structures with lateral widths below 50 nm and heights down to 15 nm, as measured via AFM (Supporting Information).

After FEBID fabrication, we used scanning and transmission electron microscopy (SEM and TEM) to characterize the geometry and composition of representative nanomagnets. Figure 1b shows an SEM top-view image of a Co NW deposit (dimensions: 14.4 μm length, 230 nm width, and 130 nm height), and Figure 1c shows a HAADF-STEM image of a cross-sectional lamella of such a deposit. Before lamella preparation, the sample was covered with a layer of Pt grown through FEBID, to protect the Co deposits while milling the lamella. Thinning and polishing of the lamella was done with an ion acceleration voltage of 30 kV and currents of 0.24 A and 83 pA respectively, resulting in a lamella thickness of ∼65 nm. In Figure 1c, the rounded cross-section of the Co NW can be discerned, as well as "halo" side-deposits extending laterally for several microns. The halo deposit in Figure 1c has a thickness of roughly 30 nm directly next to the NW, which gradually tapers off away from the NW. A selective area electron diffraction (SAED) measurement of the cross-section shown in Figure 1c indicates that the deposited Co is polycrystalline[18] (see the Supporting Information). Although hard to distinguish in the cross-sectional TEM image, the Co deposit indeed shows a granular composition, with grain sizes of roughly 2−10 nm. Such grain sizes are consistent with values found in previous works for as-deposited (nonannealed) Co FEBID structures.[18,29−31] The entire deposit is covered by an oxidized shell of roughly 8 nm thickness. Also the oxide layer has a granular composition, with lateral grain sizes of roughly 10−20 nm, corresponding well to previous findings for similar deposition parameters.[32] EDS mapping along the line cut indicated in Figure 1c reveals a composition consisting mostly of Co (82 ± 2.5 at. %), with additional smaller amounts of C (14 ± 2.5 at. %) and O (4 ± 2.5 at. %) (see Figure 1d). We find that this composition is rather uniform throughout the deposit below the surface oxide layer, including similar proportions in the halo side deposits (see the Supporting Information for additional EDS data). Interestingly, other works[19,33] report a lower Co content in the halo than in the intended deposits. The cobalt content that we find is consistent with those reported in the literature for other nonannealed Co FEBID structures.[17] As mentioned, thermal
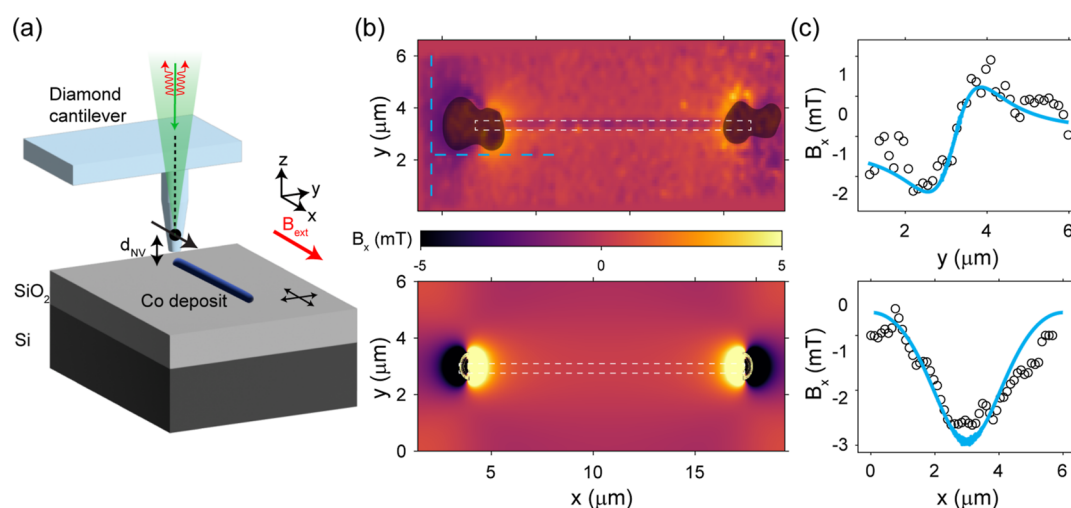
Figure 2. (a) Illustration of the SNVM setup. (b) Magnetic stray field produced by a Co NW, with B_{ext} = 202.5 mT. The rectangular area outlined by the white dashed line indicates the deposited Co NW. Top panel: SNVM data. Scan parameters: pixel size = 120 × 120 nm^2, pixel integration time = 100 ms. Data have been smoothened using a Gaussian filter with σ below pixel size. Regions over the ends of the NW have been blacked out, since here, the SNVM measurements are unreliable (see main text). Bottom panel: simulation taken at a height of 30 nm above the bottom surface of the magnet geometry. (c) Horizontal (top panel) and vertical (bottom panel) line cuts of the SNVM data, at the positions indicated by the dashed blue lines in (b). Solid blue lines are the corresponding line cuts taken from the simulated data in (b).

annealing can in principle increase this further to above 95 at. %.[19] The latter is similar to the Co content reported for other techniques such as electron-beam evaporated Co[34] but lower than what can be obtained using, for instance, MOCVD,[14] where contents of essentially 100 at. % can be obtained.

The halo is commonly deposited as a side-effect in FEBID, produced through dissociation of the adsorbed precursor by a cascade of secondary electrons generated through back-scattering of electrons off the substrate and the pattern being grown.[33,35] Such halo deposits are typically undesirable, and various approaches can be used to mitigate their formation. The amount of halo and its composition can vary depending on the deposition parameters, in particular, the exact amount of precursor gas present in the chamber. Furthermore, by performing FEBID at temperatures of −100 °C to −60 °C, halo effects can potentially be reduced. Finally, the halo can in principle be removed by means of argon ion milling (see the Supporting Information) or Xe ion beam milling,[36] although at the same time, a layer of the intended deposited structure and surrounding substrate may be removed and charge defects may be introduced into the device.

Next, we use SNVM to characterize the magnetic stray fields of our deposits. In SNVM, the Zeeman energy of the electronic spin state associated with a negatively charged NV$^-$ center defect in a diamond scanning probe is optically probed, yielding a direct measurement of the local magnetic field.[24] Compared to other scanning probe magnetometry techniques,[37] such as scanning superconducting quantum interference device (SQUID) magnetometry and magnetic force microscopy (MFM), SNVM[2,38,39] offers several advantages. Of particular relevance for our application is the high spatial resolution that can be achieved with SNVM, which can reach 15−25 nm.[37,40,41] This high resolution enables imaging of magnetic fields and currents at length scales relevant for spin qubits, magnet logic, and spintronics devices, which feature nanoscale components such as single domains, quantum dots, tunnel barriers, and nanomagnets. Also, SNVM yields quantitative measurements of the magnetic fields, as the Zeeman energy of a single NV center defect can be probed

directly. Furthermore, due to its high magnetic field sensitivity on the order of $\mu T/\sqrt{Hz}$, SNVM allows imaging the weak fields associated with nanoscale magnetic domains[42] and other spatially inhomogeneous magnetic stray fields, making it a useful tool to study the magnetization properties of FEBID Co halo structures and their impact on spin qubit performance.

Figure 2a illustrates the SNVM setup employed here: a commercial system (Qnami ProteusQ) operating under ambient conditions. We used a diamond cantilever (Qnami Quantilever MX) hosting a single negatively charged NV center embedded inside its protruding tip. The cantilever is attached to a quartz Akiyama tuning fork,[43] allowing for frequency-modulated AFM. For our measurements, we use diamond tips hosting an NV center with a spin quantization axis oriented parallel to the principal axis of the NW magnet, i.e., along the x-axis as defined in Figure 2a. This type of diamond tip is fabricated from (110) diamond substrates.[44] We estimate the distance d_{NV} of the NV center to the apex of the diamond tips to be 30−50 nm[42] and corresponding best achievable lateral spatial resolutions of 0.86 d_{NV}. During the measurements, a permanent magnet (Horiba) is used to apply an external magnetic field B_{ext} along the NV quantization axis. The magnitude and direction of the field at the sample are controlled by using a calibrated positioning of the sample with respect to this magnet. This direction coincides with the principal NW axis and its magnetic easy axis. To perform magnetometry, we employ measurements of optically detected electron spin resonance as well as of fluorescence. See, e.g., Celano et al.[42] for a more in-depth description of the SNVM setup and measurement techniques used here.

Figure 2b shows an SNVM scan of a Co NW nanomagnet, taken with B_{ext} = 202.5 mT. The scan is taken with a tip-sample distance <5 nm, and consequently the magnetometry measurements are taken at a distance ∼d_{NV} from the sample surface. The scan shows the x-component of the stray magnetic field of the NW-shaped magnet, revealing a pole at each end of the magnet. At this value of B_{ext}, the nanomagnet is almost fully saturated along its magnetic easy axis (See the Supporting

Information for a measurement taken at low B_{ext}). The associated stray field profile features large regions surrounding the nanomagnet, where field components that are transverse to the quantization axis of the NV center are small. In these regions, it is straightforward to reconstruct the x-components of the stray field from the SNVM measurements. Even so, we blacked out regions in Figure 2b in which we could not reliably track the Zeeman splitting of the NV center. This can occur when the stray magnetic field is too large, the optical read-out signal is quenched, or transverse magnetic field components are too large.[24] The latter happens especially at the ends of the NW, where strong out-of-plane stray field components are present.

We compare the SNVM measurement with finite-element simulations of the x-component of the stray field in the same area around the NW (see Figure 2b, lower panel), using the software package MuMax3.[45,46] We simulate the stray magnetic field using a magnet geometry taking into account the rounded shape of the Co NW and its halo.[47] To generate the geometry, we use an extrusion of the cross-section shown in Figure 1c; see the Supporting Information for more details. We use a typical value of the exchange constant for Co, A_{ex} = 14×10^{-12} J/m, and a $4 \times 4 \times 4$ nm^3 cell size. Using this model, we obtain a B_x stray field profile that qualitatively agrees well with the experiment, as shown in Figure 2b. Figure 2c shows plots of vertical and horizontal line cuts taken at the corresponding lines shown in Figure 2b. We find the best agreement between simulation and experiment when we use a saturation magnetization of M_s = 1.2×10^6 A/m in the simulation. Such a saturation magnetization corresponds to 85% of the bulk value, agreeing well with the atomic fraction of Co measured in our deposit (Figure 1d). We note that exactly aligning the simulation with the experimental data in the xy-plane is, to some degree, hindered by imperfect knowledge of the precise location of the NV center inside the scanning tip.

We further investigate the presence of magnetic structures of characteristic sizes of 50 to several 100s of nm. Such dimensions are relevant for applications including spin qubits, spintronics, and nanomagnet logic, which feature elements with similar length scales, for instance, quantum dots, gate electrodes, tunneling junctions, and intermagnet distances. For such applications, unintended spatial variations of stray magnetic fields can have important consequences, potentially leading to, e.g., magnetic noise, fluctuating currents, and spin qubit decoherence.[48,49]

In the Co nanomagnet devices shown here, we find small magnetic structures in the form of magnetic domains inside the NW at low B_{ext}, as well as grain-like stray fields produced by the halo deposits surrounding the NW. We investigate these structures in a Hall bar device consisting of three crossing Co NWs fabricated through FEBID using similar parameters as before (see Figure 3a). The NWs have a width of approximately 400 nm and a height of 160 nm. Figure 3b shows SNVM scans of a part of one of the Co NWs, in the region delineated in Figure 3a. The measurements shown here and in Figure 4 were taken with a diamond tip different from that used for the measurements shown in Figure 2. Due to the higher optical contrast of the NV response in this tip, we achieved a higher signal-to noise ratio on the SNVM measurements and a higher spatial resolution, making it possible to image small magnetic domains. In the upper panel of Figure 3b, SNVM data taken at B_{ext} = 240 mT are shown, at which field the magnetization of the horizontal NW section is
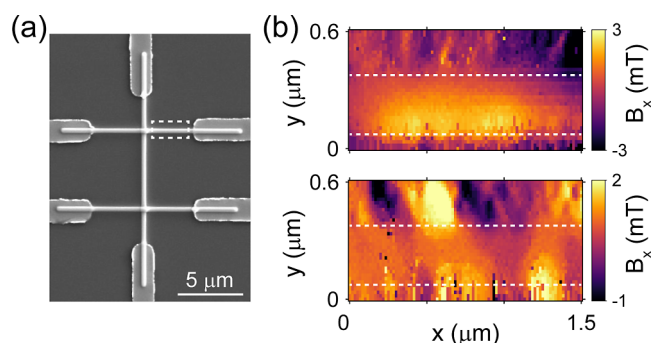

Figure 3. FEBID Co Hall bar. (a) SEM image of the Co Hall bar device patterned through FEBID. Contacts are Ti/Pd, fabricated using electron-beam lithography and a lift-off procedure. (b) SNVM maps of Co NW taken at B_{ext} = 240 mT (upper panel) and B_{ext} = 13 mT (lower panel). Scans taken in the area indicated by the dashed rectangle in (a). White dashed lines indicate the location of NW. Scan parameters: pixel size = 50×50 nm^2, pixel integration time = 100 ms.

saturated, resulting in a homogeneous stray field above the NW. In the lower panel in Figure 3b, SNVM of the same section is shown at B_{ext} = 13 mT. In this case, multiple domains of characteristic size of several hundred nanometers can be discerned in the observed stray field of the NW magnet including its halo. These domain sizes are 1 to 2 orders of magnitude larger than the grain sizes in the Co deposits and oxide layer found for the similar deposit of Figure 1c. The magnetic domains are, therefore, not clearly correlated with topographically resolved features of the deposit. Multidomain structures with these domain sizes have been observed before for NWs with similar or larger widths.[31,50] Also, Co deposits fabricated through other means than FEBID, such as MBE[15] and PLD[16] have been reported to feature magnetic domains of similar sizes, although in the form of defined stripes. Puydinger dos Santos et al.[31] find a similar mismatch between magnetic domains size and Co grain size and hypothesize that for FEBID structures, the nucleation of these magnetic domains may be induced at interfaces between Co and codeposited C. Here, we find a clear multidomain stray magnetic field profile also in the halo region, indicating the presence of magnetic material in the halo. Indeed, we find that at low B_{ext}, several domains clearly overlap both the NW deposit and the halo. This suggests that the part of the halo close to the intended deposit is similar in its composition of the magnetic material, in contrast to previous claims[19,33] but consistent with our EDS analysis showing a similar composition in the halo as in the NW (see the Supporting Information).

Next, we used SNVM to study the halo side-deposits in more detail. Figure 4a,b shows optical microscopy and SNVM images, respectively, of a Co Hall bar structure patterned via FEBID, which exhibits a significant halo side deposit. As can be seen, the halo can be distinguished as a dark shade of an inhomogeneous shape in the optical microscopy image. The SNVM image of the same area further reveals that the halo presents a stray magnetic field of granular composition (see Figure 4b) (see the Supporting Information for a magnified figure). The grainy pattern follows the same overall shape as the dark shade discernible in Figure 4a: it surrounds the intended deposit and becomes smooth further away from the deposit. We investigate the size distribution of the grainy structures using a segmentation analysis (Gwyddion) on a subset of the data shown in Figure 4b. We find a typical
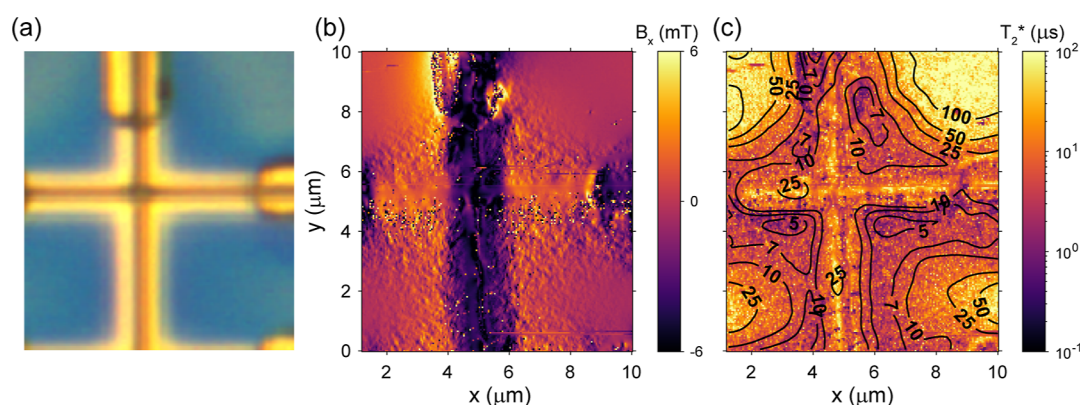
Figure 4. (a) Optical micrograph of Co Hall bar, with halo distinguishable as a dark shape. (b) SNVM map of the same area as in (a), taken at B_{ext} = 13 mT. Scan parameters: pixel size = 50×50 nm^2, pixel integration time = 100 ms. The dark vertical central line and areas at the contacts feature significant field components that are transverse to the NV quantization axis, preventing straightforward determination of B_x in these areas. (c) Map of the estimated $T_2^*(x,y)$ for the same area, assuming a spin qubit rms displacement amplitude of 10 pm.

equivalent square side a_{eq} of roughly 100 nm, larger than the pixel size of 50×50 nm^2 of the scan, and also larger than the grain sizes in the Co deposits and oxide layer found in Figure 1c. Furthermore, we find associated stray field spatial fluctuations of up to 3 mT.

Disordered stray magnetic fields, such as those in Figure 4b, can have detrimental effects on applications in spin qubits, spintronics, and nanomagnet logic. Here, we estimate the effect of such disordered stray magnetic fields on the dephasing of electron spin qubits when placed inside the stray field in Figure 4b. We refer the reader to the review of Burkard et al.[51] for an overview of the various kinds of spin qubits and their device designs. Specifically, here, we consider dephasing as a result of spin qubit displacements inside the halo stray field due to charge noise. Charge noise is one of the main mechanisms driving the decoherence of spin qubits in semiconductor quantum dots.[51] In the case of spin qubit devices with integrated nanomagnets,[49,52] charge noise can cause dephasing by randomly displacing the spins inside the field gradient of the nanomagnet. To estimate this effect, we calculate what the dephasing rate of typical electron spin qubits would be when placed in the measured disordered stray field shown in Figure 4b. Using the derivatives dB_x/dx and dB_x/dy of the stray magnetic field map of Figure 4b, we can calculate an estimate of the inhomogeneous dephasing time T_2^* for each pixel of the scan (see the Supporting Information for more details). We assume a spin qubit quantization axis along the x-axis, and realistic in-plane electron displacements of 10 pm[49] induced by charge noise. Figure 4c shows the corresponding map of $T_2^*(x,y)$. In this case, $T_2^*(x,y)$ decreases from >100 μs at the top corners of the scan, where almost no halo is present, to roughly 5 μs around the center of the scan, where the halo is most intense. We find that $T_2^* > 1$ μs for each point of the scan.

CONCLUSIONS

The estimated $T_2^*(x,y)$ values shown in Figure 4c are on par with those found for various kinds of high-quality spin qubits in Si- and Ge-based quantum dots,[53] indicating that the spatially inhomogeneous stray fields of the halo side-deposits need not limit coherence more than other factors, such as charge noise in the presence of strong intended field gradients or spin−orbit coupling and hyperfine interactions. It is worth mentioning that impurities in the FEBID deposit, such as

incorporated C or O, may contribute to charge noise, time-dependent magnetic noise, or other dephasing mechanisms. A study of such effects has not yet been made. In future work, we aim to use high-frequency SNVM measurements[54] to characterize also the time-dependent magnetic noise originating from the halo and evaluate its impact on spin qubits. Our TEM and SNVM characterization show that our FEBID structures have Co atomic content and saturation magnetization both above 80% of the bulk values. While such values would already enable large magnetic field gradients using optimized deposit geometries, past results have shown that depositions of Co content in excess of 95 atomic percent can be obtained using FEBID and purification.[17] Such high Co contents, in combination with the ability of FEBID to produce 3D magnet geometries, would enable further optimization of nanomagnets for spin qubit control.

Finally, future research may target cryo-FEBID for the patterning of magnetic nanostructures on sensitive spin qubit devices, since it allows to pattern deposits with electron doses of order 10^3 μC/cm^2, which is $\sim 10^4$ times less than that needed for FEBID at room temperature[55,56] and similar to what is used in electron-beam exposure of resists. Hence, it can be expected that sample damage due to electron irradiation is comparable for cryo-FEBID and resist-based electron-beam lithography techniques. We note that a preprint of this work has been published on arXiv.[57]

ASSOCIATED CONTENT

Data Availability Statement

The data supporting the plots of this paper are available at the Zenodo repository at https://doi.org/10.5281/zenodo.10576159.

Supporting Information

The Supporting Information is available free of charge at https://pubs.acs.org/doi/10.1021/acsanm.3c05470.

Additional experimental details, materials, and methods including additional AFM, SEM, HAADF-STEM, and SAED measurements, measurements of halo removal using Ar ion milling, additional low-field SNVM measurements of magnetic domains, schematic of simulation geometry, and detailed analysis of SNVM measurements in terms of estimated spin qubit $T_2^*(x,y)$ (PDF)

AUTHOR INFORMATION

Corresponding Author

Floris Braakman − *Department of Physics and Swiss Nanoscience Institute, University of Basel, 4056 Basel, Switzerland;* ⊙ orcid.org/0000-0003-3442-0110; Email: floris.braakman@unibas.ch

Authors

Liza Žaper − *Department of Physics, University of Basel, 4056 Basel, Switzerland; Qnami AG, 4132 Muttenz, Switzerland*

Peter Rickhaus − *Qnami AG, 4132 Muttenz, Switzerland*

Marcus Wyss − *Swiss Nanoscience Institute, University of Basel, 4056 Basel, Switzerland;* ⊙ orcid.org/0000-0001-9498-4108

Boris Gross − *Department of Physics, University of Basel, 4056 Basel, Switzerland*

Kai Wagner − *Department of Physics, University of Basel, 4056 Basel, Switzerland*

Martino Poggio − *Department of Physics and Swiss Nanoscience Institute, University of Basel, 4056 Basel, Switzerland;* ⊙ orcid.org/0000-0002-5327-051X

Complete contact information is available at:
https://pubs.acs.org/10.1021/acsanm.3c05470

Notes

The authors declare no competing financial interest.

REFERENCES

(1) Sidles, J. A.; Garbini, J. L.; Bruland, K. J.; Rugar, D.; Züger, O.; Hoen, S.; Yannoni, C. S. Magnetic Resonance Force Microscopy. *Rev. Mod. Phys.* **1995**, *67*, 249−265.

(2) Degen, C. L.; Poggio, M.; Mamin, H. J.; Rettner, C. T.; Rugar, D. Nanoscale Magnetic Resonance Imaging. *Proc. Natl. Acad. Sci. U.S.A.* **2009**, *106*, 1313−1317.

(3) Rabl, P.; Kolkowitz, S. J.; Koppens, F. H. L.; Harris, J. G. E.; Zoller, P.; Lukin, M. D. A Quantum Spin Transducer Based on Nanoelectromechanical Resonator Arrays. *Nat. Phys.* **2010**, *6*, 602−608.

(4) Gieseler, J.; Kabcenell, A.; Rosenfeld, E.; Schaefer, J. D.; Safira, A.; Schuetz, M. J. A.; Gonzalez-Ballestero, C.; Rusconi, C. C.; Romero-Isart, O.; Lukin, M. D. Single-Spin Magnetomechanics with Levitated Micromagnets. *Phys. Rev. Lett.* **2020**, *124*, 163604.

(5) Rosenfeld, E.; Riedinger, R.; Gieseler, J.; Schuetz, M.; Lukin, M. D. Efficient Entanglement of Spin Qubits Mediated by a Hot Mechanical Oscillator. *Phys. Rev. Lett.* **2021**, *126*, 250505.

(6) Slonczewski, J. C. Current-Driven Excitation of Magnetic Multilayers. *J. Magn. Magn. Mater.* **1996**, *159*, L1−L7.

(7) Gavagnin, M.; Wanzenboeck, H. D.; Belić, D.; Bertagnolli, E. Synthesis of Individually Tuned Nanomagnets for Nanomagnet Logic by Direct Write Focused Electron Beam Induced Deposition. *ACS Nano* **2013**, *7*, 777−784.

(8) Pioro-Ladrière, M.; Obata, T.; Tokura, Y.; Shin, Y.-S.; Kubo, T.; Yoshida, K.; Taniyama, T.; Tarucha, S. Electrically Driven Single-Electron Spin Resonance in a Slanting Zeeman Field. *Nat. Phys.* **2008**, *4*, 776−779.

(9) Tokura, Y.; van der Wiel, W. G.; Obata, T.; Tarucha, S. Coherent Single Electron Spin Control in a Slanting Zeeman Field. *Phys. Rev. Lett.* **2006**, *96*, 047202.

(10) Kumar, D.; Gupta, A. Evolution of Structural and Magnetic Properties of Sputtered Nanocrystalline Co Thin Films with Thermal Annealing. *J. Magn. Magn. Mater.* **2007**, *308*, 318−324.

(11) Ayadi, M.; Belhi, R.; Mliki, N.; Abdelmoula, K.; Ferré, J.; Jamet, J. P. Face Centered Cubic Cobalt Layer on Au(111): A Magneto-Optical Study. *J. Magn. Magn. Mater.* **2002**, *247*, 215−221.

(12) Kozłowski, W.; Balcerski, J.; Szmaja, W. Study of Nanocrystalline Thin Cobalt Films with Perpendicular Magnetic Anisotropy Obtained by Thermal Evaporation. *J. Magn. Magn. Mater.* **2017**, *423*, 256−261.

(13) Cerisier, M.; Attenborough, K.; Celis, J. P.; Van Haesendonck, C. Structure and Magnetic Properties of Electrodeposited Co Films onto Si(100). *Appl. Surf. Sci.* **2000**, *166*, 154−159.

(14) Ko, Y. K.; Park, D. S.; Seo, B. S.; Yang, H. J.; Shin, H. J.; Kim, J. Y.; Lee, J. H.; Lee, W. H.; Reucroft, P. J.; Lee, J. G. Studies of Cobalt Thin Films Deposited by Sputtering and MOCVD. *Mater. Chem. Phys.* **2003**, *80*, 560−564.

(15) Hehn, M.; Padovani, S.; Ounadjela, K.; Bucher, J. P. Nanoscale Magnetic Domain Structures in Epitaxial Cobalt Films. *Phys. Rev. B: Condens. Matter Mater. Phys.* **1996**, *54*, 3428−3433.

(16) Brandenburg, J.; Hühne, R.; Schultz, L.; Neu, V. Domain Structure of Epitaxial Co Films with Perpendicular Anisotropy. *Phys. Rev. B: Condens. Matter Mater. Phys.* **2009**, *79*, 054429.

(17) De Teresa, J. M.; Fernández-Pacheco, A.; Córdoba, R.; Serrano-Ramón, L.; Sangiao, S.; Ibarra, M. R. Review of Magnetic Nanostructures Grown by Focused Electron Beam Induced Deposition (FEBID). *J. Phys. D: Appl. Phys.* **2016**, *49*, 243003.

(18) Magén, C.; Pablo-Navarro, J.; De Teresa, J. M. Focused-Electron-Beam Engineering of 3D Magnetic Nanowires. *Nanomaterials* **2021**, *11*, 402.

(19) Fernández-Pacheco, A.; De Teresa, J. M.; Córdoba, R.; Ibarra, M. R. Magnetotransport Properties of High-Quality Cobalt Nanowires Grown by Focused-Electron-Beam-Induced Deposition. *J. Phys. D: Appl. Phys.* **2009**, *42*, 055005.

(20) van Kouwen, L.; Botman, A.; Hagen, C. W. Focused Electron-Beam-Induced Deposition of 3 Nm Dots in a Scanning Electron Microscope. *Nano Lett.* **2009**, *9*, 2149−2152.

(21) Silvis-Cividjian, N.; Hagen, C. W.; Kruit, P. Spatial Resolution Limits in Electron-Beam-Induced Deposition. *J. Appl. Phys.* **2005**, *98*, 084905.

(22) Salvador-Porroche, A.; Sangiao, S.; Magén, C.; Barrado, M.; Philipp, P.; Belotcerkovtceva, D.; Kamalakar, M. V.; Cea, P.; De Teresa, J. M. Highly-Efficient Growth of Cobalt Nanostructures Using Focused Ion Beam Induced Deposition under Cryogenic Conditions: Application to Electrical Contacts on Graphene, Magnetism and Hard Masking. *Nanoscale Adv.* **2021**, *3*, 5656−5662.

(23) Serrano-Ramón, L.; Córdoba, R.; Rodríguez, L. A.; Magén, C.; Snoeck, E.; Gatel, C.; Serrano, I.; Ibarra, M. R.; De Teresa, J. M. Ultrasmall Functional Ferromagnetic Nanostructures Grown by Focused Electron-Beam-Induced Deposition. *ACS Nano* **2011**, *5*, 7781−7787.

(24) Rondin, L.; Tetienne, J.-P.; Hingant, T.; Roch, J.-F.; Maletinsky, P.; Jacques, V. Magnetometry with Nitrogen-Vacancy Defects in Diamond. *Rep. Prog. Phys.* **2014**, *77*, 056503.

(25) Randolph, S. J.; Fowlkes, J. D.; Rack, P. D. Focused, Nanoscale Electron-Beam-Induced Deposition and Etching. *Crit. Rev. Solid State Mater. Sci.* **2006**, *31*, 55−89.

(26) Utke, I.; Hoffmann, P.; Melngailis, J. Gas-Assisted Focused Electron Beam and Ion Beam Processing and Fabrication. *J. Vac. Sci. Technol. B* **2008**, *26*, 1197−1276.

(27) Huth, M.; Porrati, F.; Schwalb, C.; Winhold, M.; Sachser, R.; Dukic, M.; Adams, J.; Fantner, G. Focused Electron Beam Induced Deposition: A Perspective. *Beilstein J. Nanotechnol.* **2012**, *3*, 597−619.

(28) *Nanofabrication Using Focused Ion and Electron Beams: Principles and Applications*; Utke, I., Moshkalev, S., Russell, P., Eds.; Oxford University Press: Oxford, NY, 2012.

(29) Córdoba, R.; Fernández-Pacheco, R.; Fernández-Pacheco, A.; Gloter, A.; Magén, C.; Stéphan, O.; Ibarra, M. R.; De Teresa, J. M. Nanoscale Chemical and Structural Study of Co-based FEBID Structures by STEM-EELS and HRTEM. *Nanoscale Res. Lett.* **2011**, *6*, 592.

(30) Pablo-Navarro, J.; Magén, C.; de Teresa, J. M. Purified and Crystalline Three-Dimensional Electron-Beam-Induced Deposits: The Successful Case of Cobalt for High-Performance Magnetic Nanowires. *ACS Appl. Nano Mater.* **2018**, *1*, 38–46.

(31) Puydinger dos Santos, M. V.; Brandão, J.; Dugato, D. A.; Béron, F.; Pirota, K. R.; Utke, I. Annealed Cobalt–Carbon Nanocomposites for Room-Temperature Spintronic Applications. *ACS Appl. Nano Mater.* **2020**, *3*, 7143–7151.

(32) Serrano-Ramón, L.; Fernández-Pacheco, A.; Córdoba, R.; Magén, C.; Rodríguez, L. A.; Petit, D.; Cowburn, R. P.; Ibarra, M. R.; De Teresa, J. M. Improvement of Domain Wall Conduit Properties in Cobalt Nanowires by Global Gallium Irradiation. *Nanotechnology* **2013**, *24*, 345703.

(33) Lau, Y. M.; Chee, P. C.; Thong, J. T. L.; Ng, V. Properties and Applications of Cobalt-Based Material Produced by Electron-Beam-Induced Deposition. *J. Vac. Sci. Technol.* **2002**, *20*, 1295–1302.

(34) Novaković, M.; Popović, M.; Rajić, V. Study on the Structural and Magnetic Properties of E-Beam Evaporated Co Thin Films Annealed in Vacuum. *J. Alloys Compd.* **2023**, *937*, 168411.

(35) van Dorp, W. F.; Hagen, C. W. A Critical Literature Review of Focused Electron Beam Induced Deposition. *J. Appl. Phys.* **2008**, *104*, 081301.

(36) Nikulina, E.; Idigoras, O.; Porro, J. M.; Vavassori, P.; Chuvilin, A.; Berger, A. Origin and Control of Magnetic Exchange Coupling in between Focused Electron Beam Deposited Cobalt Nanostructures. *Appl. Phys. Lett.* **2013**, *103*, 123112.

(37) Marchiori, E.; Ceccarelli, L.; Rossi, N.; Lorenzelli, L.; Degen, C. L.; Poggio, M. Nanoscale Magnetic Field Imaging for 2D Materials. *Nat. Rev. Phys.* **2022**, *4*, 49–60.

(38) Degen, C. L. Scanning Magnetic Field Microscope with a Diamond Single-Spin Sensor. *Appl. Phys. Lett.* **2008**, *92*, 243111.

(39) Schirhagl, R.; Chang, K.; Loretz, M.; Degen, C. L. Nitrogen-Vacancy Centers in Diamond: Nanoscale Sensors for Physics and Biology. *Annu. Rev. Phys. Chem.* **2014**, *65*, 83–105.

(40) Chang, K.; Eichler, A.; Rhensius, J.; Lorenzelli, L.; Degen, C. L. Nanoscale Imaging of Current Density with a Single-Spin Magnetometer. *Nano Lett.* **2017**, *17*, 2367–2373.

(41) Ariyaratne, A.; Bluvstein, D.; Myers, B. A.; Jayich, A. C. B. Nanoscale Electrical Conductivity Imaging Using a Nitrogen-Vacancy Center in Diamond. *Nat. Commun.* **2018**, *9*, 2406.

(42) Celano, U.; Zhong, H.; Ciubotaru, F.; Stoleriu, L.; Stark, A.; Rickhaus, P.; de Oliveira, F. F.; Munsch, M.; Favia, P.; Korytov, M.; Van Marcke, P.; Maletinsky, P.; Adelmann, C.; van der Heide, P. Probing Magnetic Defects in Ultra-Scaled Nanowires with Optically Detected Spin Resonance in Nitrogen-Vacancy Center in Diamond. *Nano Lett.* **2021**, *21*, 10409–10415.

(43) Suter, K.; Akiyama, T.; de Rooij, N. F.; Baumgartner, A.; Ihn, T.; Ensslin, K.; Staufer, U. Tuning Fork AFM with Conductive Cantilever. *AIP Conf. Proc.* **2003**, *696*, 227–233.

(44) Maertz, B. J.; Wijnheijmer, A. P.; Fuchs, G. D.; Nowakowski, M. E.; Awschalom, D. D. Vector Magnetic Field Microscopy Using Nitrogen Vacancy Centers in Diamond. *Appl. Phys. Lett.* **2010**, *96*, 092504.

(45) Vansteenkiste, A.; Leliaert, J.; Dvornik, M.; Helsen, M.; Garcia-Sanchez, F.; Van Waeyenberge, B. The Design and Verification of MuMax3. *AIP Adv.* **2014**, *4*, 107133.

(46) Exl, L.; Bance, S.; Reichel, F.; Schrefl, T.; Peter Stimming, H.; Mauser, N. J. LaBonte's Method Revisited: An Effective Steepest Descent Method for Micromagnetic Energy Minimization. *J. Appl. Phys.* **2014**, *115*, 17D118.

(47) Gavagnin, M.; Wanzenboeck, H. D.; Wachter, S.; Shawrav, M. M.; Persson, A.; Gunnarsson, K.; Svedlindh, P.; Stöger-Pollach, M.; Bertagnolli, E. Free-Standing Magnetic Nanopillars for 3D Nanomagnet Logic. *ACS Appl. Mater. Interfaces* **2014**, *6*, 20254–20260.

(48) Hanson, R.; Kouwenhoven, L. P.; Petta, J. R.; Tarucha, S.; Vandersypen, L. M. K. Spins in Few-Electron Quantum Dots. *Rev. Mod. Phys.* **2007**, *79*, 1217–1265.

(49) Neumann, R.; Schreiber, L. R. Simulation of Micro-Magnet Stray-Field Dynamics for Spin Qubit Manipulation. *J. Appl. Phys.* **2015**, *117*, 193903.

(50) Jaafar, M.; Serrano-Ramón, L.; Iglesias-Freire, O.; Fernández-Pacheco, A.; Ibarra, M. R.; De Teresa, J. M.; Asenjo, A. Hysteresis Loops of Individual Co Nanostripes Measured by Magnetic Force Microscopy. *Nanoscale Res. Lett.* **2011**, *6*, 407.

(51) Burkard, G.; Ladd, T. D.; Pan, A.; Nichol, J. M.; Petta, J. R. Semiconductor Spin Qubits. *Rev. Mod. Phys.* **2023**, *95*, 025003.

(52) Yoneda, J.; Otsuka, T.; Takakura, T.; Pioro-Ladrière, M.; Brunner, R.; Lu, H.; Nakajima, T.; Obata, T.; Noiri, A.; Palmstrøm, C. J.; Gossard, A. C.; Tarucha, S. Robust Micromagnet Design for Fast Electrical Manipulations of Single Spins in Quantum Dots. *Appl. Phys. Express* **2015**, *8*, 084401.

(53) Stano, P.; Loss, D. Review of Performance Metrics of Spin Qubits in Gated Semiconducting Nanostructures. *Nat. Rev. Phys.* **2022**, *4*, 672–688.

(54) Degen, C. L.; Reinhard, F.; Cappellaro, P. Quantum Sensing. *Rev. Mod. Phys.* **2017**, *89*, 035002.

(55) Bresin, M.; Toth, M.; Dunn, K. A. Direct-Write 3D Nanolithography at Cryogenic Temperatures. *Nanotechnology* **2013**, *24*, 035301.

(56) De Teresa, J. M.; Orús, P.; Córdoba, R.; Philipp, P. Comparison between Focused Electron/Ion Beam-Induced Deposition at Room Temperature and under Cryogenic Conditions. *Micromachines* **2019**, *10*, 799.

(57) Zaper, L.; Rickhaus, P.; Wyss, M.; Gross, B.; Poggio, M.; Braakman, F. Scanning NV Magnetometry of Focused-Electron-Beam-Deposited Cobalt Nanomagnets. *arXiv* **2023**, arXiv:2306.06650.